Superconductor Science and Technology

PAPER

Correlation of critical current density to quasi-biaxial texture and grain boundary cleanliness in fully dense Bi-2212 wires

To cite this article: T A Oloye *et al* 2021 *Supercond. Sci. Technol.* **34** 035018

IOP Publishing Superconductor Science and Technology
Supercond. Sci. Technol. **34** (2021) 035018 (11pp) https://doi.org/10.1088/1361-6668/abd575

Correlation of critical current density to quasi-biaxial texture and grain boundary cleanliness in fully dense Bi-2212 wires

T A Oloye[1,2,*], M Matras[4], J Jiang[1], S I Hossain[1,2], Y Su[1,5], U P Trociewitz[1], E E Hellstrom[1,2,3], D C Larbalestier[1,2,3] and F Kametani[1,2,3]

[1] Applied Superconductivity Center, National High Magnetic Field Laboratory, Florida State University, Tallahassee, FL 32310, United States of America
[2] Materials Science and Engineering, Florida State University, Tallahassee, FL 32310, United States of America
[3] Department of Mechanical Engineering, FAMU-FSU College of Engineering, Tallahassee, FL 32310, United States of America
[4] European Organization for Nuclear Research (CERN), CH-1211 Geneva, Switzerland

E-mail: ato16b@my.fsu.edu

Received 20 July 2020, revised 30 November 2020
Accepted for publication 21 December 2020
Published 2 February 2021

Abstract

The distinctive quasi-biaxial texture of $Bi_2Sr_2CaCu_2O_x$ (Bi-2212) plays an important role in enabling high critical current density (J_c) in Bi-2212 round wires (RWs). Here we studied three over pressure heat treated wires with J_c varying by a factor of ~10, all being fully dense. Using electron backscatter diffraction, we observed the differences in biaxial texture in these three wires. Transmission electron microscopy also revealed differences in grain boundary (GB) cleanliness and connectivity. These analyses showed that high J_c is unambiguously correlated to the best biaxial texture, which is in turn correlated to slow cooling from the liquid melt into solid Bi-2212. However, at 4.2 K, there is a negligible difference in intragrain pinning in the three wires, suggesting that the J_c variation by a factor of ~10 is primarily due to variable filament and intergrain connectivity. The principal determinants of intergrain connectivity is the quasi-biaxial texture and GB cleanliness. Overall, J_c optimization of the Bi-2212 RW is a complex multi-variable process, but this study shows that maximizing the biaxial texture quality is an important first step in such an optimization process.

Keywords: microscopy, superconductors, materials characterization, Bi-2212, electron backscatter diffraction EBSD, high temperature superconductors

(Some figures may appear in color only in the online journal)

1. Introduction

The future of high temperature superconductors (HTSs) is grounded in the demands of applications that often require high critical current densities (J_c) in higher fields and at higher operating temperatures [1–3] than those which can be achieved with low temperature superconductors (LTSs) [4, 5]. Among the Nb-based LTS, Nb_3Sn has been extensively developed for high field applications such as the high-luminosity (HiLumi) upgrades of the Large Hadron Collider [6]. However, the J_c of Nb_3Sn at 4.2 K falls rapidly below 1000 A mm^{-2} at 16–17 T due to its low upper critical field (H_{c2}), around 25 T at 4.2 K. Although the J_c of Nb_3Sn at 4.2 K, 16 T can be pushed up to ~3700 A mm^{-2} by introducing ZrO_2 as artificial pinning centers (APCs) or by addition of Hf or Zr to the base Nb alloy [7, 8], it will take several more years to fully implement APC in commercial Nb_3Sn conductors.

[5] Present address: Now at Materials Science and Technology Division, Oak Ridge National Laboratory, Oak Ridge, TN 37 831, USA.
[*] Author to whom any correspondence should be addressed.

HTS conductors became a viable magnet option because of their higher critical temperatures (T_c), H_{c2} and irreversibility field (H_{irr}) compared with LTS conductors. Out of many HTS materials, only a handful can be made into industrially available conductors [9, 10]. Currently, the available HTS conductor wires are made of the perovskite cuprates, REBCO ($ReBa_2Cu_3O_{7-x}$, where RE stands for rare earth), $(Bi,Pb)_2Sr_2Ca_2Cu_3O_{10+x}$ (Bi-2223) or $Bi_2Sr_2CaCu_2O_{8+x}$ (Bi-2212) [11–15]. As a long wire, REBCO and Bi-2223 can carry high J_c only when their grains are highly uniaxially or biaxially textured [11, 16, 17]. This microstructural requirement adds extra complexity to their manufacturing process and limits their wire architecture to tape forms, significantly constraining magnet design options. On the other hand, high J_c Bi-2212 has been demonstrated in macroscopically isotropic round wire (RW) form, which makes it much more compatible with the existing wind-and-react technologies used in Nb_3Sn coils [18, 19]. Like Nb–Ti and Nb_3Sn, Bi-2212 RWs can be manufactured in multiple different multi-filament architectures [20, 21]. Such unique features set Bi-2212 apart from its HTS counterparts.

Kametani *et al* compared the grain structure of Bi-2212 and Bi-2223 and found that the higher J_c in Bi-2212 RW can be attributed to its quasi-biaxial grain texture, which is naturally formed during an optimized heat treatment process [22, 23]. On slow cooling Bi-2212 from the melt state in a confined cavity such as a surrounding Ag tube, Bi-2212 tends to generate a dominant *a*-axis growth texture parallel to the filament axis because the *a*-axis grows fastest and captures off-axis grains produced by random nucleation within the filament. This dominant *a*-axis also of course defines the *b*-axis, generating the biaxial texture. However the *b*-axis (and the *c*-axis) can rotate azimuthally along and about the filament axis [22]. In addition to good texture, high J_c in Bi-2212 RW also requires fully densified filaments which is achieved by using over pressure heat treatment (OPHT), which promotes high physical filament connectivity [24, 25]. Large scale solenoids, racetrack and canted cosine theta coils have now all been successfully reacted using OPHT [26–28] and we now regard OPHT as routine. However, there is still much to learn about the details of OPHT of large coils because heating and cooling rates vary throughout any given coil structure. Furthermore, how these variations control the grain texture and grain boundary (GB) structure may vary according to the exact OPHT processing parameters [29–31], and the specific powders used in the wires. In particular, since 2016 when Engi-Mat and MetaMateria started to produce Bi-2212 powder after Nexans' exit, we have found large differences in the J_c of wires made with these new manufacturers' powders [32].

In this study, we investigated the grain structure and GB nanostructure in Bi-2212 RWs with J_c varying by a factor of ~10 using various electron microscopy techniques. High resolution electron backscatter diffraction orientation imaging microscopy (EBSD-OIM) showed that the geometrical changes in the filament cavity translate directly to the development of the Bi-2212 quasi-biaxial texture. The same scale comparison of filaments showed that the Bi-2212 texture degrades as the geometrical confinement loosens due to the growth of the Bi-2212 grains across the Ag from one filament cavity to another. Comparing transverse and longitudinal cross sections of Bi-2212 filaments, we found that the high J_c of recent Bi-2212 RWs made with the Engi-Mat powder [32] derived from strong filament confinement even with large grain growth, contributing to the development of strong *a*-axis texture and strong intergrain connectivity. Transmission electron microscopy (TEM) observation suggests that the intergrain connectivity also depends on the cleanliness of grain boundaries, which was severely degraded by the amorphous phase in our lowest J_c wire. Since we found that all three wires had the same normalized $J_c(H)$ characteristics at 4.2 K, we conclude that the wide J_c variations are primarily due to intergrain connectivity differences rather than vortex pinning differences.

2. Methods

In this study, we investigated three Bi-2212 RWs with significantly different J_c values. All powder-in tube Bi-2212 wires were made by Bruker OST [21]. The wire samples were processed at 50 bar total with 1 bar O_2 partial pressure. The schematic OPHT schedule is shown in figure 1(a). T_{max} is the maximum temperature during OPHT. The time in the melt, t_{melt} is defined as the total time that the Bi-2212 is in the melt state. The cooling rate (R_F) is the temperature slope from 874 °C to 840 °C during which the Bi-2212 re-solidification occurs. Figure 1(b) shows a representative transverse cross section of a pre-OPHT wire. The wires used in this study were made with the same 37 × 18 architecture, which is a 37 filament sub-bundle (see figure 1(c)) subsequently restacked in 18 separate filament bundles to give a total of 666 Bi-2212 filaments. The pre-OPHT wires all had the same nominal diameter of 0.8 mm.

The key processing parameters and the J_c of three Bi-2212 RWs are shown in table 1. Wires A and B were made from the same Nexans precursor powder lot 77 whose composition is $Bi_{2.17}Sr_{1.94}Ca_{0.89}Cu_{2.0}O_x$. Wire A was fast cooled (R_F = 8.0 °C h^{-1}), while wire B was slow cooled (R_F = 1.3 °C h^{-1}). The higher T_{max} of wire A gave it a longer t_{melt}. Wire C was made with Engi-Mat precursor powder LXB-52 with the composition of $Bi_{2.10}Sr_{1.90}Ca_{0.86}Cu_{2.0}O_x$. The OPHT parameters for wire C were re-optimized from wire B to accommodate for precursor powder differences as represented in table 1 [32].

For microstructural studies, transverse cross sections were prepared by sequentially polishing with SiC grinding papers, and then polished in a Buehler Vibromet using a solution of 50 nm Al_2O_3 before being imaged in a Carl Zeiss 1540 EsB scanning electron microscope (SEM). For EBSD-OIM, the wires were prepared by polishing on diamond lapping films, then ion-polishing in a JEOL cross section polisher using an argon (Ar) ion beam at 6 kV, followed by a surface-cleaning at 2 kV. EBSD of the transverse cross sections were carried out using EDAX TSL-OIM software in a Carl Zeiss 1540 EsB high resolution SEM, while the longitudinal cross sections were scanned using Oxford Aztec in a Thermo

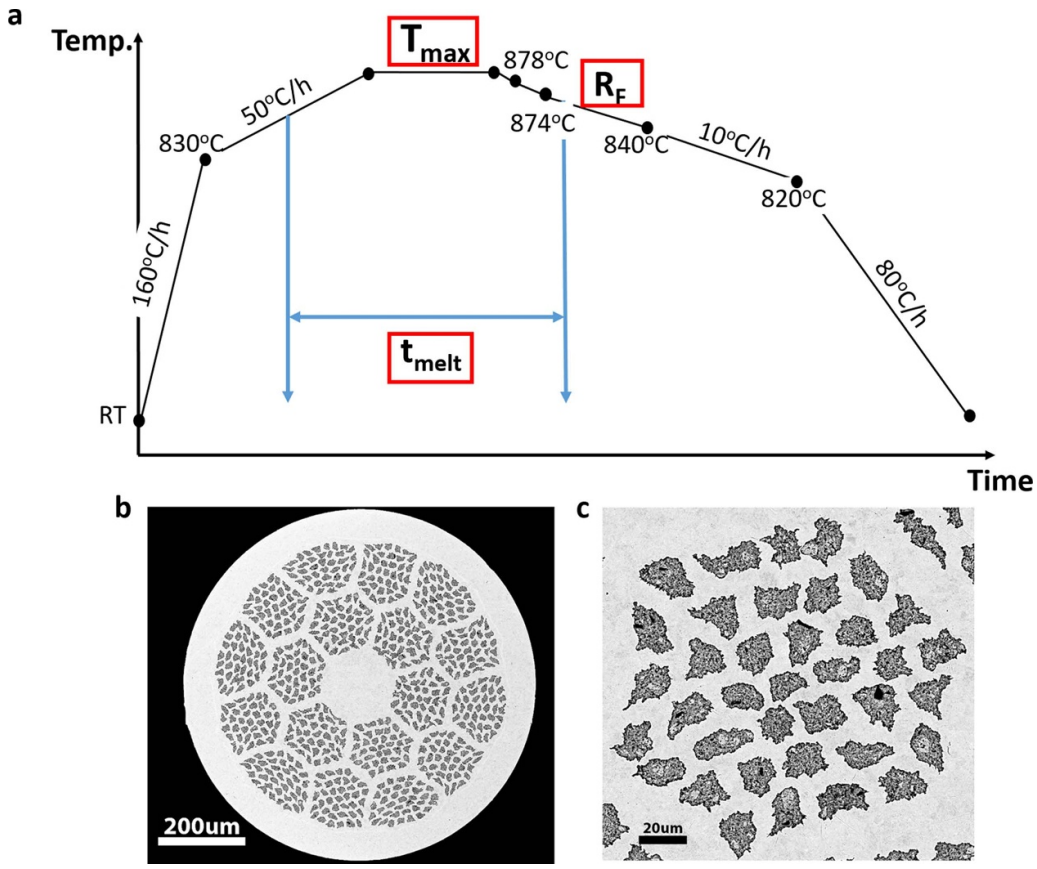

Figure 1. (a) Over pressure heat treatment (OPHT) scheme showing the important points and parameters used in the heat treatment of the three Bi-2212 RWs. The OPHT parameters highlighted here are: t_{melt}, time from which the 2212 precursor starts to melt up to the time that solidification of the 2212 grains begin; T_{max}, is the maximum temperature; R_{F} is the cooling rate; (b) transverse cross section of the unprocessed 'pre-OPHT' wire; (c) a filament bundle from an unprocessed Bi-2212 wire showing its discrete and separate filaments before OPHT.

Fisher Scientific Helios G4 high resolution SEM. (Scanning) transmission electron microscopy (S/TEM) imaging was performed in a JEOL ARM200CF atomic resolution Cs-corrected analytical TEM.

As Bi-2212 has anisotropic plate-like grains, we need both the in-plane and out-of-plane rotations to define the misorientation. Figure 2 schematically represents how these rotations appear on the inverse pole figure (IPF). As illustrated in figure 2, the Bi-2212 grain shape is $a > b \gg c$ due to the large difference in the growth rate along those axes. As a result, the b dimension of the grain is always constrained by filament cavity diameter, while the a dimension tends to grow along the filament direction [22]. For in-plane misorientation in Bi-2212 filaments, the direction of a-axis ([100]) differs along the ab-plane while keeping the c-axis direction constant, appearing as the plot spread between the [100] and [110] on the IPF plot. Meanwhile, out-of-plane misorientation only needs to change the [001] direction (c-axis) as seen in the legend below the plots. Note that [100] and [010] cannot be distinguished by EBSD, but we assign [100] to the filament direction because the growth rate is fastest (more detailed definition of IPF for Bi-2212 is discussed by Kametani *et al* [22]).

Transport critical current was measured using the four-probe method with a 1 μV cm^{-1} criterion at 4.2 K in a magnetic field of up to 15 T applied perpendicular to the wire axis. The calculation of critical current density, J_{c} was based on the area fraction of Bi-2212 filaments on the transverse wire cross section after densifying the wires by an OPHT [33]. Magnetization measurements were performed in an Oxford Instruments vibrating sample magnetometer (VSM) at 20 K in a swept field from -2 T to 14 T. These VSM measurements were used to define the Kramer field H_{K} using a linear Kramer function extrapolation to $H(0)$ in order to define H_{K}.

3. Results

For this study, we chose three Bi-2212 wires with significantly different transport J_{c} as shown in figure 3. At a field of 5 T, wire C with the Engi-Mat powder [32] (J_{c} (4.2 K, 5 T) = 9040 A mm^{-2}) had about ten times higher J_{c} than wire A (J_{c} (4.2 K, 5 T) = 927 A mm^{-2}), three times higher than wire B (J_{c} (4.2 K, 5 T) = 3140 A mm^{-2}), which was itself about three times higher than wire A. Both wires A and B were made with Nexans powder. These J_{c} differences were essentially independent of field at 4.2 K. At 15 T, J_{c} of wires A, B and C was 684 A mm^{-2}, 2362 A mm^{-2} and 6861 A mm^{-2}, respectively.

Table 1. Processing parameters and precursor powder type for the Bi-2212 round wires.

Wire ID	T_{max} (°C)	t_{melt} (h)	R_F (°C h^{-1})	J_c (A mm^{-2}) (4.2 K, 15 T)	Precursor powder
A	895.0	5.0	8.0	684	Nexans lot 77
B	892.5	3.6	1.3	2362	Nexans lot 77
C	885.5	2.6	2.5	6861	Engi-Mat LXB-52

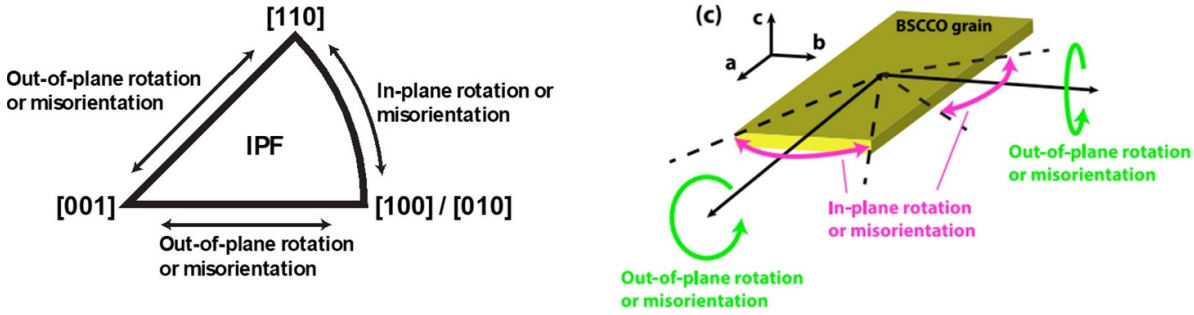

Figure 2. Inverse pole figure (IPF) plot legend used in EBSD-OIM to depict in-plane and out-of-plane grain misorientation of Bi-2212 grains [22].

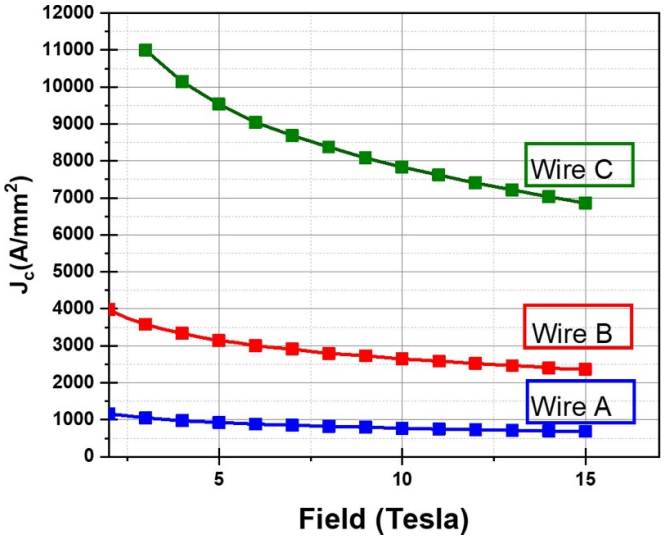

Figure 3. Transport critical current density (J_c) plots of the three wires measured at fields of 0–15 T, at $T = 4.2$ K showing their significantly different values. At 15 T; J_c (wire A) = 684 A mm^{-2}, J_c (wire B) = 2362 A mm^{-2} and J_c (wire C) = 6861 A mm^{-2}.

As shown in the Kramer plots of figure 4(a), Nexans powder wires A and B have very similar Kramer fields of 8 T at 20 K, whereas that of the Engi-Mat powder wire C is slightly higher at 9 T. It appears that the higher H_K for wire C can be attributed to its slightly different composition in the Engi-Mat. However, as our previous study indicated, such a difference in intra-grain flux pinning becomes marginal at 4.2 K [34], as indicated by figure 4(b), in which the normalized pinning force curves $F_P(H)$ are plotted as a function of field for these three wires.

Both wires A and B were made with the Nexans precursor powder, but showed ∼3.4 times difference in J_c as seen in figure 3. Figure 5 shows SEM micrographs obtained from transverse cross sections of wires A and B. Comparing the two wires, there is a clear difference in merging behavior between the filaments. The Bi-2212 filaments in wire A (figure 5(a)) are rather discrete, while wire B shows many merged filaments with common grains linking filaments (figure 5(b)). On the other hand, the 2212 grains in wire B grow and expand out of their filament cavities causing the filaments to merge with surrounding filaments significantly, altering the pre-OPHT filament cross sections shown in figure 1. There are also differences in phase assembly within the filaments as shown in the lower portion of figure 5. Wire A (figure 5(a)) shows multiple amounts of secondary phases (especially dark contrasts of alkaline earth cuprate (AEC)) within the filaments. In the filaments of wire B (figure 5(b) lower), the contrast is more uniform.

Figure 6 shows the EBSD-OIM results obtained for the transverse cross sections of representative filaments in wires A and B. The IPF maps of figure 6(a) compare filament grain structure in wires A and B on the same scale. In the IPF maps, the grain orientations are represented by colors based on crystallographic direction. As seen in the color legend, the color of green, blue and red indicate the [100] (or *a*-axis), [110, 001] (or *c*-axis), respectively. The dominance of green color in the wire A filament suggests that the Bi-2212 grains are dominantly oriented in the *a*-axis along the wire direction. On the other hand, the grains in the wire B filament mostly show a mixture of colors with green and blue, implying that the *a*-axis of the grains rotate ∼15° with respect to the filament axis.

The IPF plots are useful for approximating the degree of in-plane and out-of-plane misorientation (or rotation) of grains in the filaments. As shown in figure 6(b), the full-width-half-maximum (FWHM) of in-plane misorientation in the filament of wire A is about 15°, notably smaller than that of wire B, which is approximately 22.5°. This observation suggests that the Bi-2212 grains in wire B had a greater degree of in-plane freedom in the growth direction. Judging from the ∼15° distribution of out-of-plane misorientation in both wires,

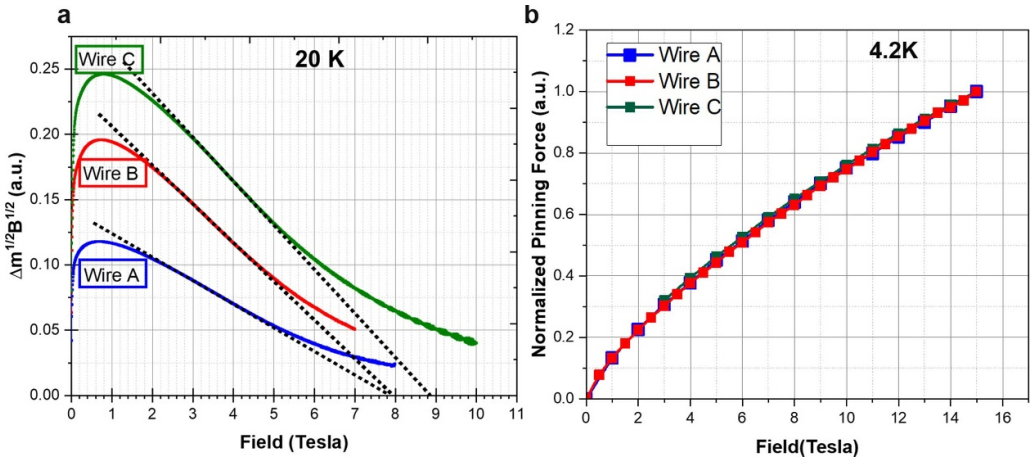

Figure 4. (a) Kramer plots at 20 K as a function of applied field for wires A, B, and C. Straight lines were drawn by fitting the linear sections of each curve, and Kramer field (H_K) is obtained from the extrapolation to the field axis. Wires A and B, both made from Nexans precursor powder have the same Kramer field ($H_K = 8$ T), while wire C made from Engi-Mat has $H_K = 9$ T. (b) Normalized pinning force curves from the transport current measurements (4.2 K) of wires A, B, and C.

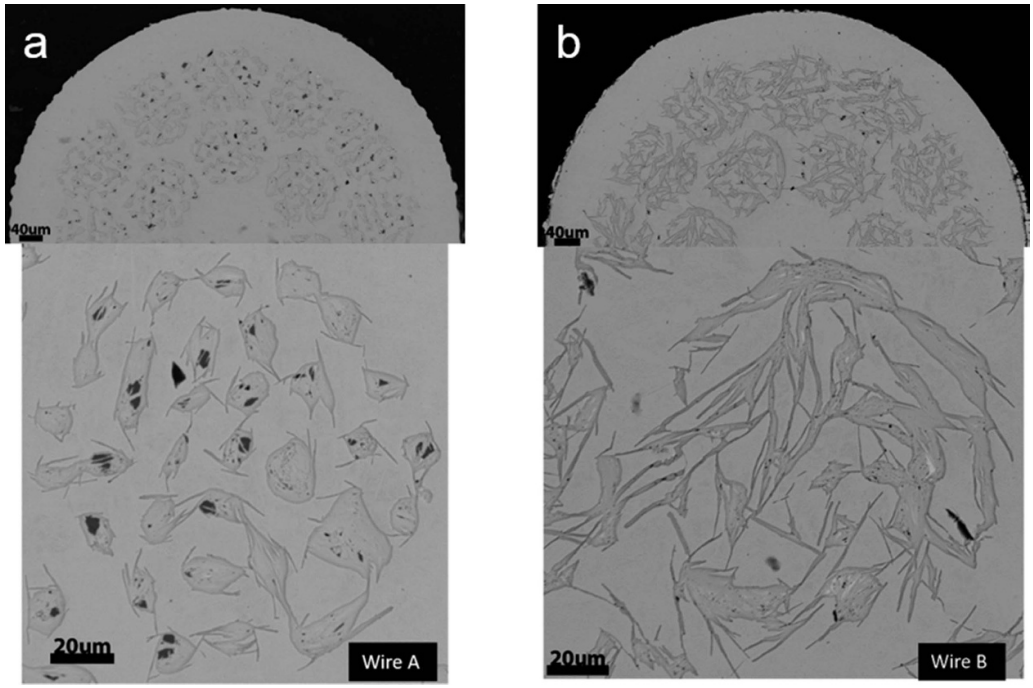

Figure 5. SEM micrographs of the transverse cross sections of: (a) wire A (J_c (5 T,4.2 K) = 927 A mm^{-2}) showing its discrete, relatively separate filaments containing significant secondary phases and; (b) wire B (J_c (5 T, 4.2 K) = 3140 A mm^{-2}) showing completely merged filaments with evidence of filament merging produced by growth across the Ag matrix. Both wires were made with Nexans precursor powder.

there is no difference in their out-of-plane misorientation. Considering the in-plane and out-of-plane misorientation on IPF, it appears that wire A developed better *a*-axis growth texture than wire B, because wire A has more of Bi-2212 grains grown along the *a*-axis as seen in the tight clustering of IPF plots around the [100] direction in figure 6(b).

The IPF data of the longitudinal cross sections of filaments in wires A and B are compared in figure 7 so as to show the differences in Bi-2212 grain texture along the longitudinal direction in the filaments. The differences in *a*-axis grain growth that were found in the transverse cross sections of figure 6 can also be seen in the longitudinal IPF cross sections of figure 7. As shown in figure 7(a), we see that wire A (top) still has more of its grains oriented in the *a*-axis (green color), unlike wire B (bottom) whose grains have a mixture of green, blue and even a few red colored areas. This shows that the grains in wire B grow with a greater amount of freedom in multiple directions, while the grains in wire A have their *a*-axis better aligned with the filament axis. The grain size in wire B is also notably longer along the longitudinal direction than that

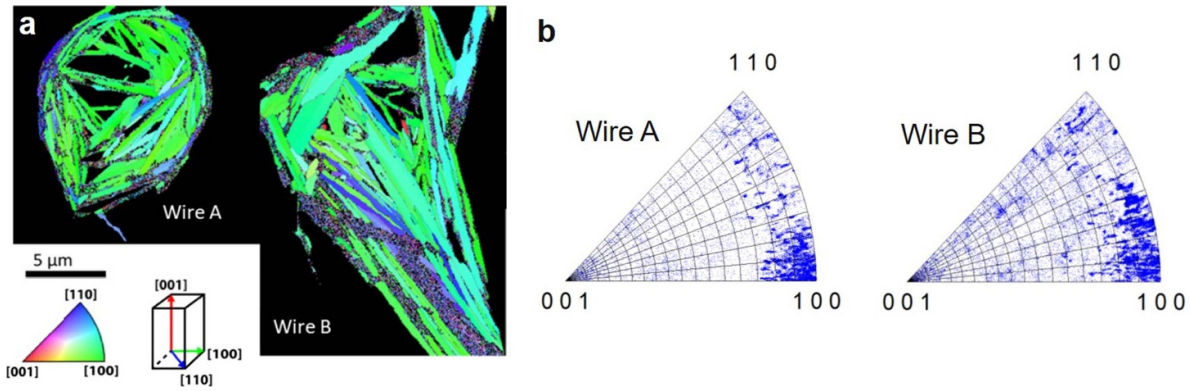

Figure 6. Grain structure and distribution of grain orientations on the transverse cross section of representative filaments in wires A and B. (a) Same scale comparison of the inverse pole figure (IPF) maps of wire A (J_c (5 T, 4.2 K) = 927 A mm^{-2}) on the left and wire B (J_c (5 T, 4.2 K) = 3140 A mm^{-2}) on the right. (b) IPF plots of wires A and B. Both of them show full-width-half-maximum (FWHM) of ∼15° in out-of-plane misorientation. But wire A has a narrow spread in in-plane misorientation (∼15°) than wire B having FWHM of ∼22.5° in in-plane misorientation.

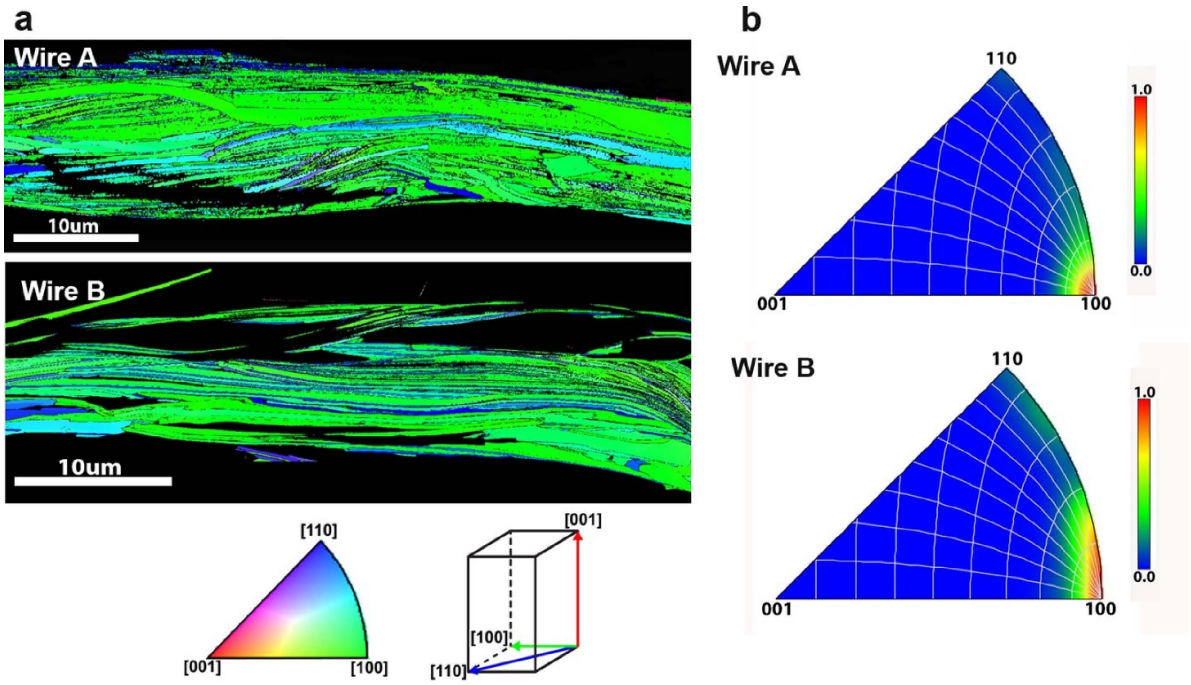

Figure 7. (a) Inverse pole figure (IPF) map on the longitudinal cross section of representative filament in wires A and B. The IPF is constructed using the projection axis parallel to the filament direction. The majority of its grains in wire A are oriented in the [100] direction (green colored), whereas more grains oriented toward the [110] direction (bluish colored) are present in wire B. (b) IPF color temperature plots of wires A and B. Wire A shows a narrower intensity spread (FWHM: ∼10°) around the [100] direction than wire B which has a broader spread of intensity (FWHM: ∼20°) toward [110].

of wire A. The IPF plots are represented as a color temperature map in figure 7(b). Note that the Aztec software used for the longitudinal EBSD represents the IPF plot rather differently compared with the TSL-OIM software used for the transverse cross sections. Unlike the transverse IPF done with TSL-OIM, the grain orientation on the longitudinal IPF of figure 7(b) that was derived by Aztec is represented by color temperature with red being the most intense, followed by yellow, green and then blue being zero intensity of plot. In figure 7(b), the IPF plot for wire A (top) shows that most of grains are highly aligned along the *a*-axis ([100] direction) within 10° of FWHM, represented by the tight and sharp intensity of red around the [100] corner of the IPF plot. Wire B (figure 7(b)—bottom) has a greater spread of grain orientations as indicated by the broader spread of approximately 20° toward [110].

Previous work has suggested that the strong *a*-axis biaxial texture is essential for high J_c in the Bi-2212 RWs [22]. The EBSD analysis of transverse and longitudinal cross sections presented in figures 6 and 7 suggest that wire A has better texture than wire B. The transport J_c of wire A, however, is markedly lower than that of wire B, as seen in figure 3. The scanning transmission electron microscope (STEM) images of

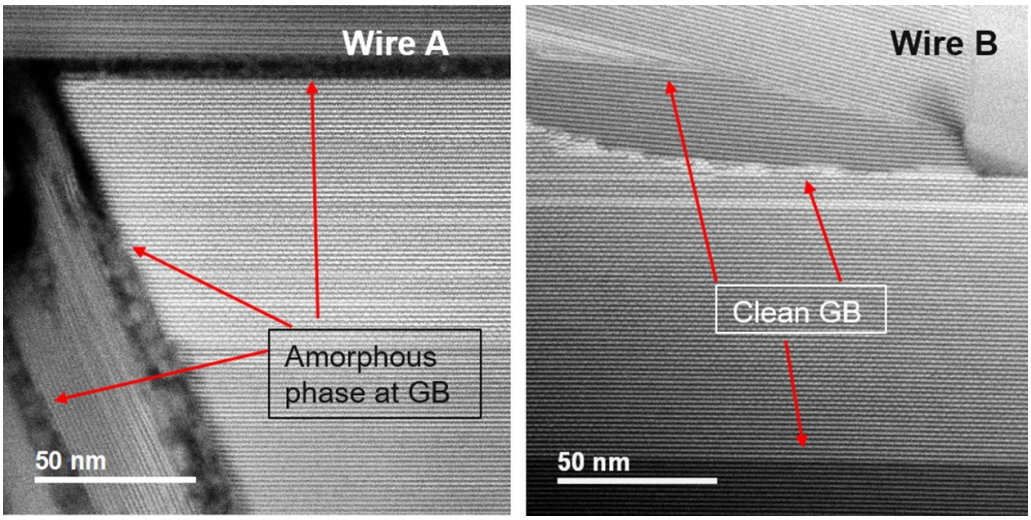

Figure 8. Scanning transmission electron microscope (STEM) images showing the grain boundaries of wires A and B. Wire A has the amorphous phase at its grain boundaries, whereas the grain boundaries are clean in wire B.

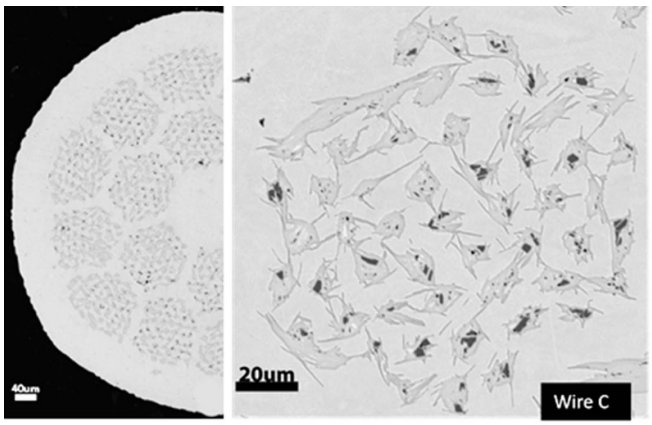

Figure 9. SEM of the transverse cross section of wire C made from Engi-Mat precursor powder showing relatively discrete filaments. The dark contrasts in the filaments are the alkaline earth cuprate (AEC) secondary phase.

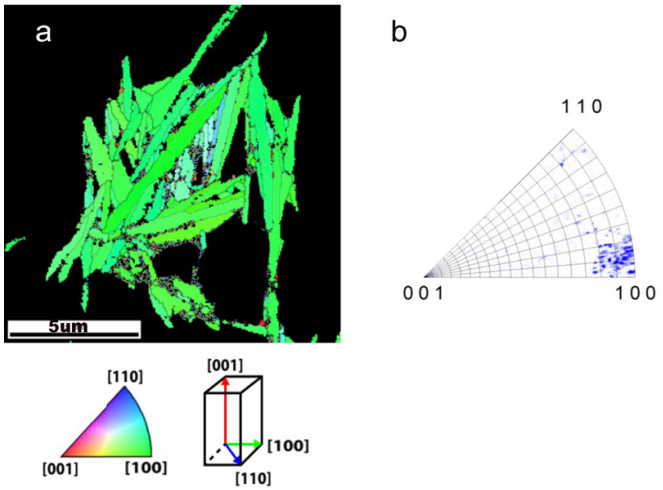

Figure 10. The grain structure and distribution of grain orientations across the transverse cross section of a representative filament in wire C. (a) IPF map showing that almost all Bi-2212 grains are colored green, indicating strong *a*-axis ([100]) alignment. (b) IPF plot representing the narrow spread (FWHM: ∼10°) of its in-plane and out-of-plane misorientations.

figure 8 compare the GB structure in wires A and B. In wire A, an amorphous phase can be seen at the GBs as the dark, blurred contrast, physically decoupling the Bi-2212 grains in wire A. It is considered that this amorphous phase is left over from the melt that was unable to re-solidify into Bi-2212 due to the fast rate of cooling in wire A. In contrast, the grain boundaries in wire B are clean and its grains are well connected. These STEM results suggest that lack of intergrain connectivity due to the amorphous layer at the GBs is responsible for the observed low J_c of wire A despite its a strong *a*-axis texture.

Figure 9 shows the transverse cross section of wire C, which had the highest J_c of the three wires. In the SEM micrograph of figure 9, the filaments in wire C are rather discrete, although they are partly connected by whisker-shaped grains as described earlier by Shen *et al* [35]. Wire C also has much less distortion and intergrowth of single grains from filament to filament of the type seen in wire B (figure 5(b)). Some of the filaments in wire C appear to contain more secondary phases (shown as the dark gray contrasts) than wire B.

Figure 10 represents the IPF map and plot on the transverse cross sections of representative filament in wire C. The IPF map of figure 10(a) reveals that almost all grains are growing in the [100] direction (green color dominant), and the IPF plot of figure 10(b) shows a low FWHM (∼10°) of both in-plane and out-plane misorientation, clearly indicating the high alignment of Bi-2212 *a*-axis along the filament direction. The tight confinement of grain orientations around the [100] corner on the IPF plot clearly represents the strong *a*-axis texture in wire C with the highest J_c. In comparison, wire B with the intermediate J_c has a larger misorientation in the in-plane direction as seen in figure 6(b).

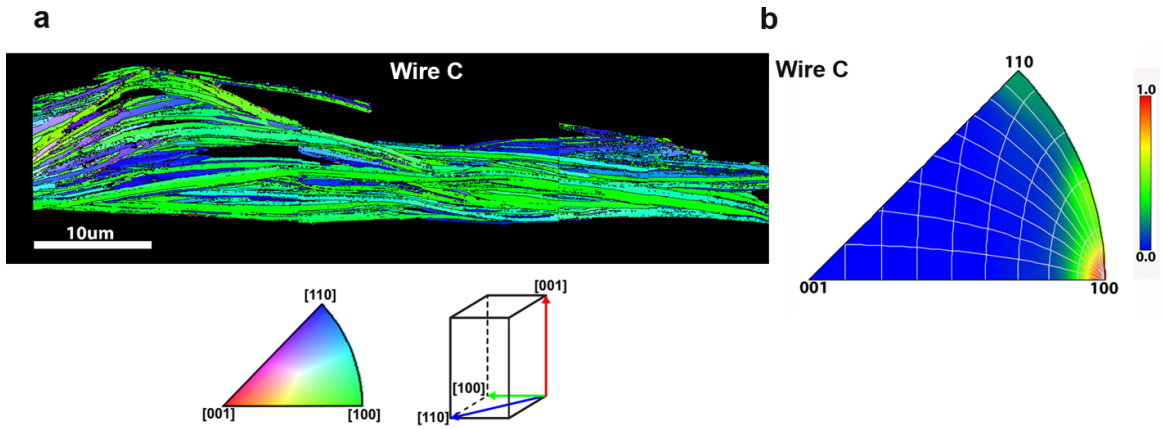

Figure 11. EBSD-OIM on the longitudinal cross section of a representative filament in wire C. (a) IPF map of the Bi-2212 grain structure with predominantly green colored [100] grains with a few blue/purple grains in the [110] direction. (b) IPF color temperature plot with the projection axis parallel to the filament direction, showing 10° in-plane misorientation (with minor spread up to 20°) and ∼10° out-of-plane misorientation.

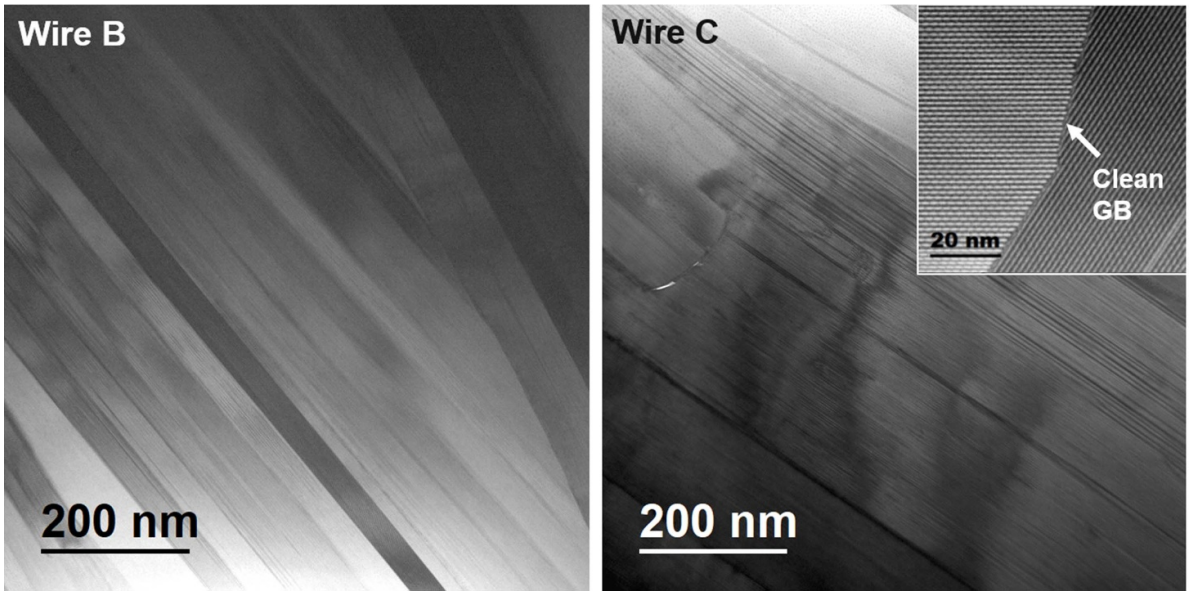

Figure 12. TEM images of transverse cross sections of wire B and wire C. The average thickness of Bi-2212 grains is ∼53 nm and ∼150 nm in wires B and C, respectively. Both wires show well-connected and clean grain boundaries. The inset of STEM image of wire C shows a representative structure of clean grain boundaries.

The IPF of the longitudinal cross section of wire C shown in figure 11 is consistent with the strong *a*-axis texture depicted in the transverse cross section of figure 10. The IPF map of figure 11(a) shows the Bi-2212 grains in wire C with a predominantly green color with some minor grains with color slightly varying between green and blue, indicating that the grains in wire C are *a*-axis oriented along the filament direction. The IPF plot of wire C in figure 11(b) also shows that the grain orientations are concentrated around [100], judging from the sharp and high plot intensity represented as the red color around [100]. The minor spread toward [110] in green on the IPF plot (figure 11(b)) indicates that a small number of grains are misoriented along the in-plane direction. Nonetheless, comparing the color distribution of IPF plots between wire B (figure 7(b)) and wire C (figure 11(b)), wire C clearly has the stronger *a*-axis texture along the filament direction than wire B. Comparing figure 7(a)—bottom and figure 11(a), the length of Bi-2212 grains along the longitudinal direction appears very similar between wires B and C.

The bright field TEM micrographs of figure 12 shows the transverse cross section of representative filaments in wires B and C. As the sharp and well-defined contrasts of GBs in the TEM image and the inset of atomic resolution STEM show in figure 12, the GBs in wire C do not show trace of amorphous phase as seen in wire A, and are as clean and well connected as those in wire B. This side-by-side comparison also reveals the differences in the thickness of Bi-2212 grains in the two wires. Consistent with the grain structure observed in the SEM micrographs (figure 5(b)) and EBSD-OIM IPF map of the transverse cross section (figure 6(a)—right), the

Bi-2212 grains in wire B appear thinner than those of wire C. Upon analysis of multiple grains, the average thickness of the Bi-2212 grains in a representative cross section of wire B was found to be ∼53 nm, while that of wire C was ∼150 nm, about three times larger.

4. Discussion

In this study, we selected three Bi-2212 RWs with large differences in J_c by a factor of ∼10. Our results strongly suggested that the large J_c variation in those wires is determined not by intragrain flux pinning, but essentially by intergrain connectivity, for which the degree of quasi-biaxial texture and the GB cleanliness both play a vital role. Indeed wire C which has the highest J_c of any Bi-2212 RWs till date [32] exhibited the strongest intergrain connectivity defined by the highest degree of quasi-biaxial texture and clean GBs.

Concerning the intragrain flux pinning, the Kramer field (H_K) at 20 K obtained from the magnetization showed about 1 T difference between the wires made with the Nexans and Engi-Mat powder (figure 4(a)). The powder differences are explained in greater detail by Jiang *et al* [32]. Wires A and B, both of which were made from Nexans precursor powder but had rather different OPHT parameters both have similar H_K of about 8 T, indicating that the intragrain pinning is essentially insensitive to the OPHT parameters. Regarding the powder composition, we found that the Engi-Mat powder LXB-52 used for this study is slightly Cu-rich compared with Nexans [32]. It is plausible that the ∼9 T of H_K in wire C resulted from the slight difference in the powder composition or in the powder synthesis method used at Engi-Mat [28], although we do not fully understand how the powder composition affects H_K. Judged by figure 4(b), the intragrain flux pinning at 4.2 K is identical over the field range of 0–15 T that we used for the transport J_c measurements. Thus, we conclude that the large J_c difference observed here is not derived from the variation of intragrain flux pinning [3, 22, 35].

Our previous work strongly suggested that the geometrical confinement of the narrow filament cavity is vital in order to develop the quasi-biaxial texture of Bi-2212 grains [22]. It was considered that the microstructure with the least filament merging is the most effective for the strong texture formation because the discrete filament cross sections most effectively align the Bi-2212 grain growth direction along the filament direction. In this aspect, comparing the SEM transverse cross sections of wires A, B and C (figures 5 and 9), one might predict that wire A would develop the highest J_c since it appears to have the least filament merging. Indeed, wire A developed the strong *a*-axis growth texture as seen in figure 6. However, wire A has the lowest J_c, which is only about 10% of the highest J_c of wire C, implying that there is another cause to J_c degradation. The STEM micrograph of figure 8 revealed that wire A has a significant amount of amorphous phase at its grain boundaries (GB), disconnecting the individual grains to reduce the supercurrent paths. It is suggested that the significantly fast cooling rate ($R_F = 8$ °C h^{-1}) used for wire A did not allow the complete re-solidification of Bi-2212 phase from the melt during OPHT, leaving a residual melt phase as the insulating amorphous phase at the GBs [33]. In contrast, the grain boundaries in wires B and C were found to be clean and well connected, supposedly because the melt phase could fully transform into Bi-2212 with a small amount of solid second phases from the markedly slower R_F (1.3 °C h^{-1} and 2.5 °C h^{-1} for wires B and C, respectively) compared with that for wire A. We conclude that the GBs disconnected by the amorphous layers is the central cause of the lowest J_c of wire A despite having the least filament merging.

The comparison of wires B and C, both of which have clean GBs, probably represents the actual J_c correlation to grain texture. As we discussed earlier, the intragrain pinning difference which might be caused by the different precursor powder can be ignored at 4.2 K below 15 T. Thus, it is considered that the large J_c increment of wire C with respect to wire B is largely due to the improvement of quasi-biaxial grain texture. The grain misorientation in wire C is approximately 10° for both in-plane and out-of-plane, which is significantly improved compared with wire B. In particular, the in-plane misorientation in the transverse cross section is significantly improved from ∼22.5° in wire B to ∼10° in wire C. In both samples, the adequately slow R_F promotes the growth of large Bi-2212 grains by reducing the frequency of heterogeneous Bi-2212 nucleation during the re-solidification from the melt. Under the geometrical constraint from the Ag cavity wall, only the Bi-2212 grains whose fastest-growing *a*-axis fits in the long filament cavities continue to grow, while the nuclei of highly misaligned grains are consumed by such growing grains. Comparing the filament structure of wires B and C (figures 5(b) and 9), wire C has markedly less filament merging than wire B. It appears that the more defined filament cross section contributes to form the better texture in wire C than in wire B due to the stronger constraint to the growing direction of Bi-2212 grains.

The reason for the defined filament structure in wire C has not been fully understood yet. According to the previous work by Jiang *et al* [32], the particle size of the AEC 14:24 phase is smaller in the Engi-Mat powder which might help reduce sausaging during wire drawing. This could also improve filament uniformity along the length in wire C during the wire fabrication and OPHT [32]. Furthermore, the T_{max} is 7 °C lower and the t_{melt} is 1 h shorter for wire C than for wire B as seen in table 1. These factors might contribute to the reduced filament bonding, and possibly increase the number of filaments that provide the proper geometrical confinement for strong *a*-axis growth texture.

As seen figure 1, the OPHT profile has many variables that can influence the microstructure and J_c. The recent change of powder manufacturer from Nexans to Engi-Mat required the readjustment of some of the OPHT parameters that resulted in the record high J_c [32]. Although the Engi-Mat powder contributes to bring our record J_c (6861 A mm^{-2} at 4.2 K, 15 T) of wire C, those OPHT readjustments and the powder change made it difficult to fully correlate each OPHT parameter to the biaxial texture formation. Nevertheless, our results provide the important insights regarding how the OPHT parameters influence the microstructure. In the design-of-experiments study,

Matras *et al* identified three key OPHT parameters (T_{max}, t_{melt}, R_F) that control J_c in Bi-2212 RW [31]. As discussed earlier, our results show that the appropriate R_F is necessary to form the clean GBs and the extensive *a*-axis grain growth. Matras found that T_{max} and t_{melt} strongly affects the filament merging in the fully processed wires. Shen *et al* pointed out that a longer t_{melt} leads to more filament merging [29]. However, wire A with the longest t_{melt} of 5 h shows much less filament bonding compared with wire B with the 62% shorter t_{melt} (3.6 h) as seen in figure 5. A possible explanation is that the fast cooling rate (R_F) of wire A did not allow the Bi-2212 grains to grow through the Ag wall and reach the adjacent filaments from their initial (pre-OPHT) filament cavities, coincidently suppressing filament merging even under the long t_{melt} which, instead, left many GBs disconnected by the residual liquid phase that ultimately brought J_c down ~90% from wire C. This indicates that the degree of filament merging is not determined just by t_{melt}, but presumably by a combination of T_{max}, t_{melt}, R_F and/or the other OPHT parameters.

This study clearly showed that the highest J_c of recent Bi-2212 RWs can be correlated to the enhanced intergrain connectivity that is defined by the formation of strong quasi-biaxial texture and clean GBs. The formation of this biaxial texture was found in the essentially discrete filaments. However, further microstructural studies are required to fully understand how the filament structure is affected by the OPHT parameters and the wire fabrication. Maintaining the filaments as discrete as possible appears to be a key factor to form the strong texture, but we need a full systematic study to detangle the complex OPHT and fabrication process so that we can fully control the filament structure and grain texture formation in the Bi-2212 RWs.

5. Conclusion

By utilizing advanced microscopy techniques, we investigated the microstructure of three Bi-2212 RWs with differences of up to ten times in J_c. The 4.2 K intragrain flux pinning in those wires are almost identical, suggesting the large J_c difference is essentially caused by variations in the filament or intergrain connectivity. We identified the strong *a*-axis growth, quasi-biaxial texture, and clean grain boundaries (GBs) as the primary factor for high J_c. The wire with the GBs blocked by the amorphous phase exhibits the lowest J_c despite having the least amount of filament merging, suggesting that the GBs must be clean before establishing the effect of biaxial texture on J_c. We conclude that, with clean GBs, the highest J_c ever reported correlates to the strongest quasi-biaxial texture within a discrete, not merged filament structure.

Acknowledgments

This work is supported by the US Department of Energy Office of High Energy Physics under the Grant Number DE-SC0010421 and by National High Magnetic Field Laboratory, which is supported by National Science Foundation under the Award Number DMR-1644779, and by the State of Florida, and is amplified by the U.S. Magnet Development Program (MDP). We are grateful to E Bosque, Y Kim and the Bi-2212 conductor and coil group members at the Applied Superconductivity Center for their valuable discussions.

ORCID iDs

T A Oloye https://orcid.org/0000-0003-3497-5351
M Matras https://orcid.org/0000-0003-4613-2837
E E Hellstrom https://orcid.org/0000-0001-8263-8662
D C Larbalestier https://orcid.org/0000-0001-7098-7208
F Kametani https://orcid.org/0000-0002-1067-9331

References

[1] Tenbrink J, Wilhelm M, Heine K and Krauth H 1991 Development of high-T/sub c/superconductor wires for magnet applications *IEEE Trans. Magn.* **27** 1239–46
[2] Rossi L and Bottura L 2012 Superconducting magnets for particle accelerators *Rev. Accel. Sci. Technol.* **05** 51–89
[3] Larbalestier D C *et al* 2014 Isotropic round-wire multifilament cuprate superconductor for generation of magnetic fields above 30 T *Nat. Mater.* **13** 375–81
[4] Godeke A, Jewell M C, Fischer C M, Squitieri A A, Lee P J and Larbalestier D C 2005 The upper critical field of filamentary Nb_3Sn conductors *J. Appl. Phys.* **97** 093909
[5] Godeke A 2006 A review of the properties of Nb_3Sn and their variation with A15 composition, morphology and strain state *Supercond. Sci. Technol.* **19** R68
[6] Bottura L, de Rijk G, Rossi L and Todesco E 2012 Advanced accelerator magnets for upgrading the LHC *IEEE Trans. Appl. Supercond.* **22** 4002008
[7] Balachandran S, Tarantini C, Lee P J, Kametani F, Su Y, Walker B, Starch W and Larbalestier D 2019 Beneficial influence of Hf and Zr additions to Nb4at%Ta on the vortex pinning of Nb_3Sn with and without an O source *Superconductor Science and Technology* **32** 7
[8] Xu X, Sumption M D and Peng X 2015 Internally oxidized Nb_3Sn strands with fine grain size and high critical current density *Adv. Mater.* **27** 1346–50
[9] Bednorz J G, Takashige M and Müller K A 1987 Susceptibility measurements support high-Tc superconductivity in the Ba–La–Cu–O system *EPL* **3** 379–86
[10] Müller K A and Bednorz J G 1987 The discovery of a class of high-temperature superconductors *Science* **237** 1133–9
[11] Trociewitz U P *et al* 2011 35.4 T field generated using a layer-wound superconducting coil made of $(RE)Ba_2Cu_3O_{7-x}$ (RE = rare earth) coated conductor *Appl. Phys. Lett.* **99** 202506
[12] Flukiger R *et al* 1992 High critical current densities in Bi(2223)/Ag tapes *Supercond. Sci. Technol.* **5** S61–S68
[13] Li Q, Brodersen K, Hjuler H A and Freltoft T 1993 Critical current density enhancement in Ag-sheathed Bi-2223 superconducting tapes *Physica* C **217** 360–6
[14] Sato K *et al* 1991 Transport current properties of silver-sheathed BiPbSrCaCuO wire and coil *Cryogenics* **31** 687–9
[15] Yao X and Shiohara Y 1997 Large REBCO single crystals: growth processes and superconducting properties *Supercond. Sci. Technol.* **10** 249–58
[16] Desgardin G, Monot I and Raveau B 1999 Texturing of high-Tc superconductors *Supercond. Sci. Technol.* **12** R115–33

[17] Grasso G, Perin A and Flükiger R 1995 Deformation-induced texture in cold-rolled Ag sheathed Bi(2223) tapes *Physica* C **250** 43–49
[18] Miao H, Huang Y, Hong S, Gerace M and Parrell J 2014 Bi-2212 round wire development for high field applications *J. Phys.: Conf. Ser.* **507** 022020
[19] Marken K R, Miao H, Meinesz M, Czabaj B and Hong S 2003 BSCCO-2212 conductor development at Oxford Superconducting Technology *IEEE Trans. Appl. Supercond.* **13** 3335–8
[20] Miao H, Meinesz M and Czabaj B 2008 Microstructure and J_c improvements in multifilamentary Bi-2212⁄Ag wires for high field magnet applications *AIP* ed J Parrell and S Hong 423–30
[21] Miao H, Marken K R, Meinesz M, Czabaj B and Hong S 2005 Development of round multifilament Bi-2212/Ag wires for high field magnet applications *IEEE Trans. Appl. Supercond.* **15** 2554–7
[22] Kametani F, Jiang J, Matras M, Abraimov D, Hellstrom E E and Larbalestier D C 2015 Comparison of growth texture in round Bi2212 and flat Bi2223 wires and its relation to high critical current density development *Sci. Rep.* **5** 8285
[23] Martinelli A, Bellingeri E, Leveratto A, Leoncino L, Ritter C and Malagoli A 2018 *In situ* x-ray and neutron diffraction investigation of Bi-2212 in multifilamentary wires during thermal treatment *Phys. Rev. Mater.* **2** 084801
[24] Jiang J *et al* 2011 Doubled critical current density in Bi-2212 round wires by reduction of the residual bubble density *Supercond. Sci. Technol.* **24** 082001
[25] Kametani F *et al* 2011 Bubble formation within filaments of melt-processed Bi2212 wires and its strongly negative effect on the critical current density *Supercond. Sci. Technol.* **24** 075009
[26] Zhang K *et al* 2018 Tripled critical current in racetrack coils made of Bi-2212 Rutherford cables with overpressure processing and leakage control *Supercond. Sci. Technol.* **31** 105009
[27] Chen P *et al* 2017 Experimental study of potential heat treatment issues of large Bi-2212 coils *IEEE Trans. Appl. Supercond.* **27** 1–5
[28] Shen T *et al* 2019 Stable, predictable and training-free operation of superconducting Bi-2212 Rutherford cable racetrack coils at the wire current density of 1000 A/mm 2 *Sci. Rep.* **9** 1–9
[29] Shen T, Jiang J, Kametani F, Trociewitz U P, Larbalestier D C and Hellstrom E E 2011 Heat treatment control of Ag–$Bi_2Sr_2CaCu_2O_x$ multifilamentary round wire: investigation of time in the melt *Supercond. Sci. Technol.* **24** 115009
[30] Shen T, Li P and Ye L 2018 Heat treatment control of Bi-2212 coils: I. Unravelling the complex dependence of the critical current density of Bi-2212 wires on heat treatment *Cryogenics* **89** 95–101
[31] Matras M 2016 Investigation of Ag-sheathed multi-filamentary $Bi_2Sr_2CaCu_2O_{8-x}$ superconducting round wires processed with overpressure, for high field magnets PhD (Florida, US: The Florida State University) pp 53–58 (available at: https://search.proquest.com/docview/1864738033/abstract/A94590DAC8EF4828PQ/1)
[32] Jiang J *et al* 2019 High-performance Bi-2212 round wires made with recent powders *IEEE Trans. Appl. Supercond.* **29** 1–5
[33] Matras M R, Jiang J, Trociewitz U P, Larbalestier D C and Hellstrom E E 2020 Process to densify $Bi_2Sr_2CaCu_2O_X$ round wire with overpressure before coil winding and final overpressure heat treatment *Supercond. Sci. Technol.* **33** 025010
[34] Brown M D 2018 Mechanical and electrical characterization of critical current density in round and rectangular reinforced $Bi_2Sr_2CaCu_2O_{8+X}$ wires for high field magnet applications PhD (Florida, US: The Florida State University) pp 89–93 (available at: https://diginole.lib.fsu.edu/islandora/object/fsu%3A661125/)
[35] Shen T *et al* 2010 Filament to filament bridging and its influence on developing high critical current density in multifilamentary $Bi_2Sr_2CaCu_2O_x$ round wires *Supercond. Sci. Technol.* **23** 025009